⌘ *Author's Choice*

THE JOURNAL OF BIOLOGICAL CHEMISTRY VOL. 285, NO. 42, pp. 32446–32457, October 15, 2010

Structural Insights into Serine-rich Fimbriae from Gram-positive Bacteria*[S]

Received for publication, March 29, 2010, and in revised form, June 25, 2010 Published, JBC Papers in Press, June 28, 2010, DOI 10.1074/jbc.M110.128165

Stéphanie Ramboarina[‡1,2], James A. Garnett[‡1], Meixian Zhou[§], Yuebin Li[§], Zhixiang Peng[§], Jonathan D. Taylor[‡], Wei-chao Lee[‡], Andrew Bodey[‡], James W. Murray[‡], Yilmaz Alguel[‡], Julien Bergeron[‡¶], Benjamin Bardiaux[‖], Elizabeth Sawyer[‡], Rivka Isaacson[‡], Camille Tagliaferri[‡], Ernesto Cota[‡], Michael Nilges[**], Peter Simpson[‡], Teresa Ruiz[‡‡], Hui Wu[§3], and Stephen Matthews[‡4]

From the [‡]Department of Biological Sciences, Centre for Structural Biology, Imperial College London, South Kensington, London SW7 2AZ, United Kingdom, the [§]Department of Pediatric Dentistry, University of Alabama at Birmingham, Birmingham, Alabama 35294-0007, the [¶]Department of Infectious Diseases, King's College London School of Medicine, London SE1 9RT, United Kingdom, the [‖]Structural Biology Unit, Leibniz Institute for Molecular Pharmacology, FMP Robert-Rossle Strasse 10, 13125 Berlin, Germany, the [**]Institut Pasteur Unité de Bioinformatique Structurale, 25-28 Rue du Dr Roux, F-75724 Paris Cedex 15, France, and the [‡‡]Department of Molecular Physiology and Biophysics, University of Vermont, Burlington, Vermont 05405

The serine-rich repeat family of fimbriae play important roles in the pathogenesis of streptococci and staphylococci. Despite recent attention, their finer structural details and precise adhesion mechanisms have yet to be determined. Fap1 (Fimbriae-associated protein 1) is the major structural subunit of serine-rich repeat fimbriae from *Streptococcus parasanguinis* and plays an essential role in fimbrial biogenesis, adhesion, and the early stages of dental plaque formation. Combining multidisciplinary, high resolution structural studies with biological assays, we provide new structural insight into adhesion by Fap1. We propose a model in which the serine-rich repeats of Fap1 subunits form an extended structure that projects the N-terminal globular domains away from the bacterial surface for adhesion to the salivary pellicle. We also uncover a novel pH-dependent conformational change that modulates adhesion and likely plays a role in survival in acidic environments.

Biofilms offer protection to bacteria from hostile environments, such as adverse temperatures, pH, and attack by other organisms, including their hosts (1). Significant progress has been made toward understanding which gene products are involved in biofilm formation. Fimbriae, which are long, thin filamentous structures that decorate bacterial surfaces, are often employed in the reversible adhesion to surfaces at the early stages of biofilm formation (2). A large number of chronic bacterial infections involve the formation of a biofilm, with the development of dental plaque being one of the most familiar and diverse (3).

The commensal streptococci of the oral cavity play a major role in the foundation of dental plaque (4). These include early colonizers of the tooth surface, viridans *Streptococcus sanguinis,* and *Streptococcus parasanguinis*, which serve as substratum for the subsequent adhesion of other microflora, such as cariogenic *Streptococcus mutans*, and periodontal pathogens *Porphyromonas gingivalis* and *Aggregatibacter actinomycetemcomitans* (5). In addition, both *S. sanguinis* and *S. parasanguinis* have been described as etiological agents in infective endocarditis (6–10) with the formation of streptococcal biofilms being central to the development of disease. Fap1 (Fimbriae-associated protein 1) has been identified as the major structural subunit of *S. parasanguinis* fimbriae and is essential for fimbrial biogenesis, adhesion, and biofilm formation (11–15). Fap1-like subunits assemble into a new family of fimbriae in Gram-positive bacteria (16), which are characterized by large polypeptides (>200 kDa) comprising an extensive region of glycosylated, serine-rich repeats (SRR)[5] flanked by a unique N-terminal region and a C-terminal cell wall-anchoring domain. The SRR family of fimbriae plays direct roles in several bacterial diseases, including the pathogenesis of streptococcal (17) and staphylococcal infective endocarditis (18), streptococcal meningitis (19), invasive pneumococcal disease (20), and neonatal disease (21, 22).

Fap1 from *S. parasanguinis* provides a model system to study bacterial adhesion and biofilm formation by this poorly understood family of proteins. Furthermore, these adhesins play a major role in early stages of dental plaque formation. Despite recent attention, the finer structural details of SRR fimbriae and their adhesion mechanisms have yet to be determined. Combining multidisciplinary, high resolution structural studies with

* This work was supported, in whole or in part, by National Institutes of Health Grants R01DE017474 (to T. R.) and R01DE011000 and R01DE017954 (to H. W.). This work was also supported by Wellcome Trust Program Grant 079819 and Equipment Grant 085464 (to S. M.).

⌘ *Author's Choice*—Final version full access.

[S] The on-line version of this article (available at http://www.jbc.org) contains supplemental Figs. S1–S9.

The atomic coordinates and structure factors (codes 2x12 and 2kub) have been deposited in the Protein Data Bank, Research Collaboratory for Structural Bioinformatics, Rutgers University, New Brunswick, NJ (http://www.rcsb.org/).

[1] Both authors contributed equally to this work.

[2] Present address: Dept. of Molecular and Cellular Interactions, VIB Structural Biology Brussels, Vrije Universiteit Brussel, Pleinlaan 2, B-1050 Brussels, Belgium.

[3] To whom correspondence may be addressed. E-mail: hwu@uab.edu.

[4] To whom correspondence may be addressed. E-mail: s.j.matthews@imperial.ac.uk.

[5] The abbreviations used are: SRR, serine-rich repeat; HSQC, heteronuclear single quantum coherence; SAXS, small angle x-ray scattering; UA, uranyl acetate; PTA, phosphotungstic acid; MAT, methylamine tungstate; SHA, saliva-coated hydroxylapatite; PDB, Protein Data Bank.

biological assays, we provide new insights into adhesion by Fap1. We propose a model in which the serine-rich repeats of Fap1 subunits form an extended structure that projects the N-terminal globular domains away from the bacterial surface for adhesion to the salivary pellicle. We also uncover a novel pH-dependent conformational change that modulates adhesion and likely plays a role in survival in acidic environments.

EXPERIMENTAL PROCEDURES

Protein Preparation—Recombinant Fap1-NR (residues 106–437), Fap1-NR$_\alpha$ (residues 116–231), and Fap1-NR$_\beta$ (residues 231–437) were expressed using pRSETA plasmid (Promega) in the BL21(DE3) *Escherichia coli* strain (Novagen). Unlabeled proteins were produced in LB media, and isotopically ^{15}N- and ^{13}C-labeled proteins were produced in M9 minimal medium supplemented with $^{15}NH_4Cl$ and [^{13}C]glucose. A $^{2}H/^{15}N/^{13}C$ triple labeled Fap1-NR sample was produced from Silantes media in *E. coli* CDN OD1. Selenomethionine-labeled Fap1-NR protein was expressed in methionine auxotroph B834 grown in minimal media supplemented with selenomethionine. All samples were purified using nickel affinity chromatography followed by size exclusion chromatography on a Superdex-75 column (GE Healthcare). NMR samples were concentrated to 0.1–0.2 mM in 50 mM PBS, pH 8, 50 mM NaCl. X-ray diffraction samples were concentrated to ~8 mg/ml and stored at −72 °C in 20 mM Tris-HCl, pH 7.5, 100 mM KCl. Small angle x-ray scattering samples were gel-filtered in 50 mM PBS, pH 5 or 8, 50 mM NaCl immediately prior to data collection.

NMR Spectroscopy—NMR measurements were performed at 303 K on ^{15}N,^{13}C-labeled Fap1-NR$_\alpha$ and Fap1-NR$_\beta$ domain samples in 50 mM PBS buffer, pH 8.0, 50 mM NaCl. NMR experiments for backbone and side-chain assignment on Fap1-NR$_\alpha$ were performed on two different Bruker spectrometers, a DRX500 and an Avance II 800, equipped with cryoprobe. Assignments were completed using standard triple-resonance assignment methodology (23). NOE data for structure calculations of Fap1-NR$_\alpha$ were obtained from an 800-MHz edited ^{1}H-^{15}N nuclear Overhauser effect spectroscopy-heteronuclear single quantum coherence (NOESY-HSQC) and a 950-MHz edited ^{1}H-^{13}C NOESY-HSQC experiments with a mixing time of 100 ms recorded on a 950-MHz Oxford superconducting magnet. ^{15}N T_1 and T_2 relaxation times on a ^{15}N-labeled Fap1-NR$_\alpha$ sample at pH 8 were recorded at 800 MHz, and the T_1/T_2 ratio was measured for each residue.

^{1}H-^{15}N and $^{1}H^{\alpha}$-C^{α} residual dipolar coupling constants were measured using two-dimensional in-phase anti-phase ^{15}N-^{1}H-HSQC (24) and three-dimensional HN(CO)CA experiments, respectively, on ^{15}N,^{13}C-labeled Fap1-NR$_\alpha$ sample at pH 8 partially aligned in Pf1 filamentous phage media. ^{15}N-^{1}H TROSY-HSQC spectra of ^{15}N-^{2}H-labeled Fap1-NR were recorded at pH 5, 6, and 8 at 800 MHz. A series of ^{15}N-^{1}H HSQC on Fap1-NR$_\alpha$ at different pH values from pH 5 to 8 were performed at 500 and 950 MHz. ^{15}N-^{1}H HSQC on Fap1-NR$_\beta$ domain was performed at 800 MHz.

^{1}H-^{15}N TROSY NMR experiments (25) were performed at 303 K on a uniformly ^{15}N,^{13}C,^{2}H-labeled Fap1-NR on a Bruker Avance II 800 equipped with a cryoprobe. TROSY versions of HNCACB and HN(CO)CACB experiments for backbone assignment allowed us to assign ~50% assignment of Fap1-NR spectra. All NMR data were processed using NMRpipe (26) and analyzed with NMRView (27).

NMR Structure Determination—The ARIA protocol for automated NOESY assignment interfaced with the CNS program was used for structure calculation (28–30). Secondary helical structure in Fap1-NR$_\alpha$ was first identified using the chemical shift-based dihedral angle prediction software TALOS (31). For residues located in helices, hydrogen bonds, ϕ and ψ backbone dihedral angles derived from TALOS and residual dipolar couplings, were introduced as restraints in the ARIA structure calculation. 38 D_{NH} and 54 $D_{C\alpha H\alpha}$ residual dipolar couplings spread evenly among the three helices were used for structure calculation. Axial Da and rhombic R components were initially estimated using the histogram method from the normalized distribution of these 92 residual dipolar couplings (32). The axial (Da = −3.0 Hz) and rhombic (R = 0.55) components of the alignment tensor were further optimized with the program MODULE (33) based on the precalculated structures. For NOE-derived and hydrogen bond distance restraints, a log harmonic potential was used for the second Cartesian cooling phase of the simulated annealing, and the weight on the restraints was iteratively updated (34). The final average weights were 6.8 kcal/mol/Å^2 for NOE restraints and 25 kcal/mol/Å^2 for hydrogen bond restraints. To avoid distortion of the peptide group during Cartesian cooling, high force constants were used to maintain planarity, whereas low force constants were employed for residual dipolar coupling restraints. Furthermore, the final structures were carefully inspected for local distortions. 100 conformers were calculated in the final iteration, and 10 lowest energy structures were refined in a shell of water molecules (35). A summary of NMR-derived restraints and statistics on the ensemble of the NMR structure is reported in Table 2. The solution structure of the Fap1-NR$_\alpha$ domain was deposited in the Protein Data Bank with PDB ID code 2kub.

Crystallization, Data Collection, and Structure Determination—Crystals of both native and selenomethionine-labeled Fap1-NR were grown at 297 K using the hanging drop vapor diffusion method in 0.1 M Hepes over a range of pH values from pH 6.5 to 8.0, 5% 2-methyl-2,4-pentanediol, 10–12.5% PEG 6K, and 9–12.5 mM spermine-tetra-HCl. Crystals were briefly soaked in the mother liquor supplemented with 20% PEG 6K before cryocooling. Selenomethionine-labeled Fap1-NR data were collected at the selenium peak energy, determined by a fluorescence scan, at beamline ID29 at the European Synchrotron Radiation Facility in Grenoble, France. Data were processed using MOSFLM and scaled with SCALA (36). Two selenium sites were located using SHELXD (37), and then phases were calculated using AUTO-SHARP. Two monomers were located in the electron density, and a model was built into the averaged solvent flattened experimental map using COOT (38), with rounds of refinement in REFMAC5 (39). The final model was refined with NCS restraints and TLS groups, with 5% of the reflections omitted for cross-validation. Statistics of data collection and the final model are shown in Table 1. The coordinates and structure factors have been deposited in the PDB under accession code 2x12.

Small Angle X-ray Scattering (SAXS)—SAXS data were recorded at the X33 beamline of EMBL (DESY, Hamburg, Germany). Samples of Fap1-NR buffered at either pH 5 or 8 and at 1.3, 2.7, and 4.5 mg/ml were measured using 120-s exposures to synchrotron radiation. The range of q values measured was from 0.07 to 0.48 $Å^{-1}$. SAXS data were processed in the standard manner using the program PRIMUS (40). Data points across all three concentrations were merged (points 1–300, 250–600, and 550–2000 were derived from the low, medium, and high concentration samples, respectively). The radius of gyration (R_g) and scattering at zero angle ($I(0)$) were calculated from the analysis of the Guinier region by AUTORG. The distance distribution function ($P(r)$) was subsequently obtained using GNOM, yielding the maximum particle dimension (D_{max}). An ensemble of 20 low resolution *ab initio* structures were calculated using the program GASBOR utilizing default parameters (41). Models were then aligned and averaged by DAMAVER. The known atomic resolution structures of the α and β domains were docked into the low resolution bead model of Fap1-NR at pH 8 by the program SITUS (42). This was achieved by splitting the bead model into two halves and independently minimizing the fit between the high and low resolution structures.

Site-directed Mutagenesis of Fap1 of S. parasanguinis—Surface regions containing an abundance of exposed hydrophobic amino acid side chains were selected for mutation. The hydrophobic residues together with selected hydrophilic side chains were mutated individually to alanine using the Stratagene QuikChange® mutagenesis system as described previously (43). This included Ile-134, Glu-138, Asp-142, Leu-163, and Val-164 in Fap1-NR_α together with Leu-385, Ile-291, Leu-292, Leu-300, Asn-403, Gln-405, and Ile-411 in Fap1-NR_β. In brief, the full-length *fap1* gene cloned into an *E. coli* and streptococcal shuttle vector pVA838 was used as a template. Site-directed mutagenesis PCR was carried out to construct a series of alanine replacement mutants of *fap1* using the mutagenic oligonucleotide primers that corresponded to the changes of selected amino acid residues to alanine residues. The amplified mutant plasmids were transformed into competent *E. coli* following the instructions by a QuikChange® XL mutagenesis kit (Stratagene, La Jolla, CA). The plasmids with designed mutations were purified; the mutated region was sequenced to ensure the accuracy of the site-directed mutagenesis. The wild-type and mutant plasmids were then transformed into a *fap1* mutant of *S. parasanguinis*. Fap1 expression was monitored by Western blot analysis using an antibody against mature Fap1 (F51).

Adhesion of S. parasanguinis to SHA, an In Vitro Tooth Model—Adhesion of *S. parasanguinis* to saliva-coated hydroxylapatite (SHA) was performed as described previously (11). In brief, cells of wild-type *S. parasanguinis* and site-directed mutants were labeled with 2 μCi of [*methyl*-^{3}H]thymidine/ml. The radiolabeled bacteria were incubated with SHA beads at 37 °C for 1 h to allow bacterial binding to occur and then washed. Supernatants and washed beads were transferred to scintillation vials, and their respective radioactivities were determined and used to calculate adhesion percentage as described previously. In all assays, a wild-type strain FW213 and the *fap1*-

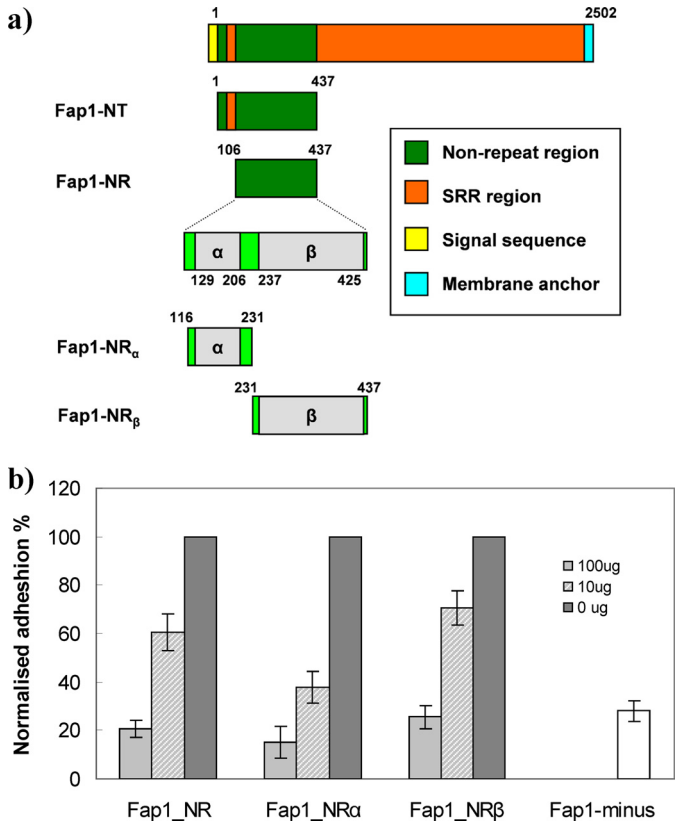

FIGURE 1. **Domain organization of *S. parasanguinis* Fap1 and adhesion to SHA.** *a*, schematic representation of the domain structure of Fap1. The amino acid positions at which the domains begin and end are indicated. Mature Fap1 is numbered 1–2502. *b*, Fap1-NR, Fap1-NR_α, and Fap1-NR_β block bacterial adhesion in a dose-dependent manner. 0, 10, and 100 μg of recombinant Fap1 proteins were preincubated with SHA before adding [^{3}H]thymidine-labeled wild-type *S. parasanguinis*. Wild-type binding is normalized to 100%, and the *fap1* deletion mutant was used as a negative control.

TABLE 1

Crystal data collection and refinement statistics for Fap1-NR_β

Numbers in parentheses refer to the outermost resolution shell.

Crystal parameters	
Space group	$P3_2\,2\,1$
Cell dimensions	$a = b = 108.67$ Å $c = 126.25$ Å
Data collection	
Beamline	ESRF ID29
Wavelength	0.97910 Å
Resolution	2.90 Å (2.90-3.06 Å)
Unique observations	19,567 (2832)
R_{meas} [a]	0.132 (0.47)
$\langle I\rangle/\sigma I$	15.2 (4.16)
Completeness	99.84% (100.0%)
Redundancy	7.88 (7.53)
Refinement	
R_{work} [b]/R_{free} [c]	21.10%/25.05%
No. of protein residues	400
r.m.s.d. stereochemistry [d]	
Bond lengths	0.02 Å
Bond angles	1.8°
Ramachandran analysis [e]	
Residues in outlier regions	2% (Ser-246 A and B chain)
Residues in favored regions	377 (95.2%)
Residues in allowed regions	394 (99.5%)

[a] $R_{meas} = \Sigma(h)(\sqrt{(n_h/(n_h-1))}\Sigma(l)|I_{hl} - \langle I_h\rangle|/\Sigma(h)\Sigma(l)\langle I_h\rangle$, where I is the integrated intensity of a given reflection, $\langle I\rangle$ is the mean intensity of multiple corresponding symmetry-related reflections, and n_h is the number of observations of reflection h.
[b] $R_{work} = \Sigma||F_o| - |F_c||/\Sigma F_o$, where F_o and F_c are the observed and calculated structure factors, respectively.
[c] $R_{free} = R_{work}$ calculated using ~5% random data excluded from the refinement.
[d] Root mean square deviation (r.m.s.d.) stereochemistry is the deviation from ideal values.
[e] Ramachandran analysis was carried out using Molprobity (85).

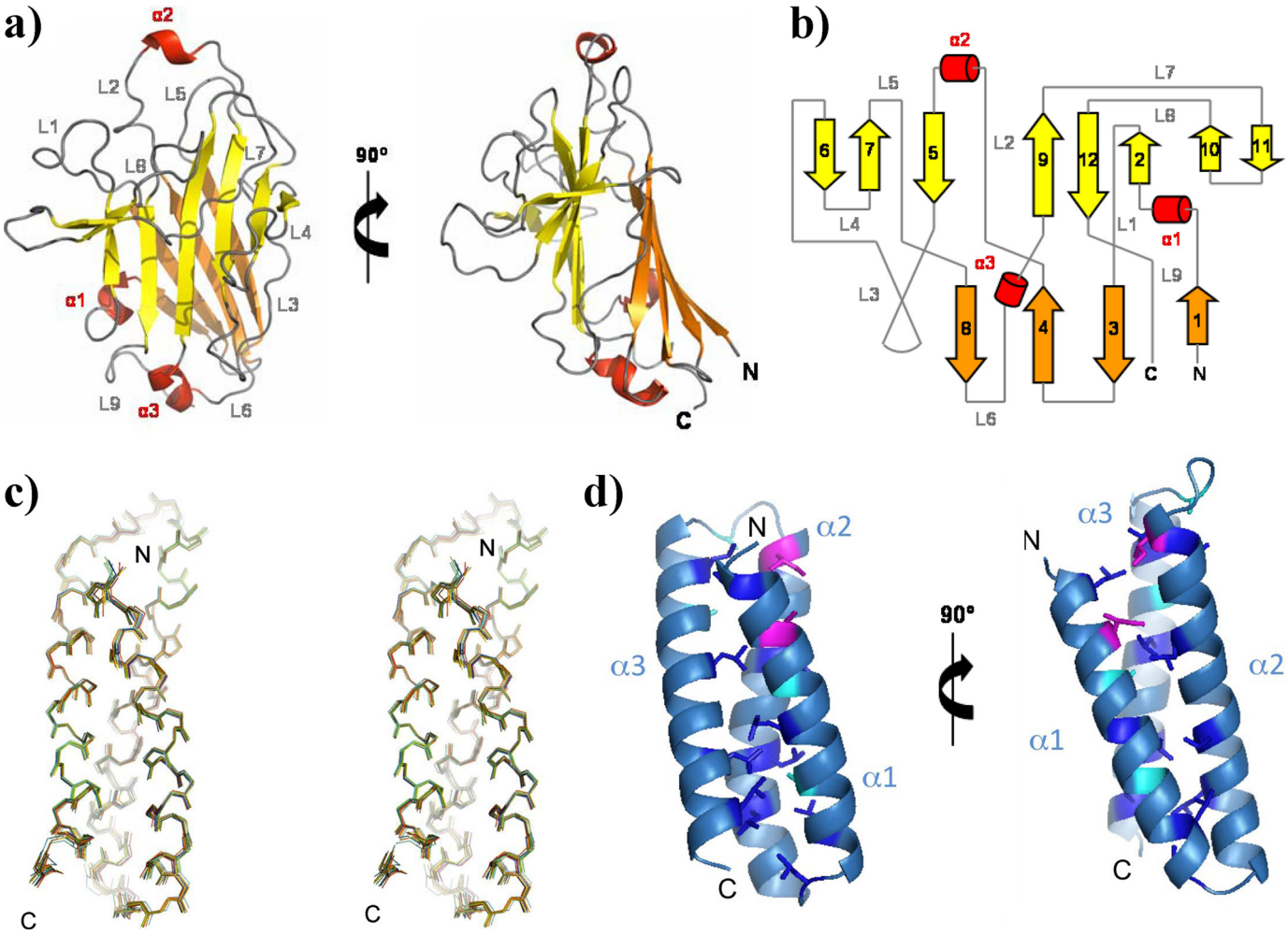

FIGURE 2. **Three-dimensional structures of the two subdomains Fap1-NR$_\alpha$ and Fap1-NR$_\beta$ from the major nonrepeat region from *S. parasanguinis* Fap1 fimbriae.** *a,* ribbon representation of the x-ray structure of Fap1-NR$_\beta$. The β-strands are colored in *yellow* and *orange* and short helices in *red*. *L1* to *L9* refer to loops 1 to 9 in the structure. *b,* topology diagram of the x-ray structure of Fap1-NR$_\beta$ with the same colored code as in *a*. *c,* superimposition of the 10 best NMR structures of Fap1-NR$_\alpha$ with the three helices α1, α2, and α3 shown in *blue*. *d,* ribbon representation of the NMR structure of Fap1-NR$_\alpha$ in two different orientations with the three helices α1, α2, and α3 in *blue*. Leucine, alanine, and isoleucine side chains involved in inter-helix interactions are colored in *dark blue*, *cyan*, and *magenta*, respectively.

minus mutant were used as positive and negative controls, respectively.

Adhesion Blocking Assays—Wild-type *S. parasanguinis* cells were labeled with 2 μCi of [^{3}H]thymidine/ml. The radiolabeled cells were treated and reconstituted as described previously. Recombinant Fap1-NR, Fap1-NR$_\alpha$, and Fap1-NR$_\beta$ were expressed and purified as described previously. The purified recombinant proteins were dialyzed overnight against the adhesion buffer and added into SHA beads that were equilibrated with adhesion buffer and then incubated at 37 °C for 1 h on a rotating shaker. The treated SHAs were incubated with labeled *S. parasanguinis* and subjected to the adhesion assay described above.

Electron Microscopy—*S. parasanguinis* (FW213) was grown from frozen stocks preserved with 5% dimethyl sulfoxide (44). Frozen cells were streaked onto blood agar plates and incubated aerobically for 12–15 h in 5% CO_2 at 37 °C. Broth cultures were prepared by inoculation of single colonies from the blood agar plates into flasks containing Todd-Hewitt Broth (THB) and grown statically under aerobic conditions. 5-ml cell cultures in early exponential phase (A_{470} ~0.4) were centrifuged at 4000 × *g* to remove the media. Cell pellets were resuspended in 100 μl of PBS (100 mM phosphate buffer, pH 7.4, 150 mM NaCl) at 4 °C.

Samples were diluted in PBS to the appropriate concentration for electron microscopy studies. A small aliquot (5 μl) was applied to 400 mesh copper grids coated with a thin carbon film. The grids were washed by running several drops of PBS buffer over them and negatively stained by subsequently running a few drops of the staining solution (1% uranyl acetate (UA; Ted Pella, Redding, CA), 2% phosphotungstic acid, pH 7, with NaOH (Ted Pella), and 2% methylamine tungstate (MAT; Nanoprobes, Yaphank, NY) over the grids. The last drop of stain was left on the grid for 30 s; the excess liquid was wicked off, and the grids were fast air dried. The grids were observed using a dual axis tomography holder (Fischione Instruments, Export, PA) on a Tecnai 12 electron microscope (FEI Co., Hillsboro, OR) equipped with an LaB6 cathode (Kimball Physics Inc., Wilton, NH) operated in point mode, and a 14-μm 2048 × 2048 CCD camera (TVIPS, Germany). The microscope was run under identical conditions as have been used in the past to

obtain images that show Thon rings beyond 0.9 nm resolution in vitreous ice preparations (45). Negatives were recorded at an accelerating voltage of 100 kV and nominal magnification of ×52,000 under low dose conditions on S0-163 Kodak film (~1000 e^-/nm^2). Negatives were scanned with 7 μm raster size on a Zeiss flat bed scanner (Intergraph, Huntsville, AL). The images were converted for processing with the SPIDER image processing system (46) and reduced two times to a final pixel size of 0.27 nm at the specimen level. A contrast transfer function correction was performed on the images by calculating the averaged periodogram of each image and fitting to it the theoretical transfer function calculated by varying the defocus value and astigmatism parameters (angle and strength) (47). Each image was corrected by multiplying it with a modified version of its transfer function (47).

Straight filament regions, which showed no overlap, were boxed with the program "helixboxer" in the EMAN image processing package (48). Images containing 55 nm filament sections were windowed using the SPIDER image processing system (46). The unevenness of the background was removed using the "ramp" command, and the intensities were normalized to zero average (5 pixels strips along the longitudinal edge of the images were used to calculate the average intensity value of the background). A power spectrum was calculated from each image, and an averaged power spectrum was calculated for each stain condition. The averaged power spectra were visualized using the WEB display program (46), and the height of the layer lines was extracted.

RESULTS

Major Nonrepeat Region of Fap1 Blocks S. parasanguinis Adhesion to SHA—Recently, SRR fimbrial proteins known to interact with salivary components and human platelets have also been identified in other medically relevant streptococcal and staphylococcal species (49). Interestingly, the sequences of regions outside the serine repeats are implicated in adhesion and poorly conserved among the family (50–53). To define the minimal region responsible for Fap1 adhesion to the salivary pellicle, the nonrepeat portion from the N terminus of Fap1 (Fap1-NR, residues 106–437; Fig. 1*a*) was recombinantly produced in *E. coli*, purified using metal affinity chromatography, and tested for its ability to inhibit *S. parasanguinis* adhesion to an *in vitro* tooth model, SHA. Binding assays revealed a dose-dependent decrease in binding in the presence of recombinant Fap1-NR indicating that this region of Fap1 is able to competitively block adhesion (Fig. 1*b*).

Limited trypsin proteolysis of Fap1-NR released two stable domains corresponding to a C-terminal 25-kDa polypeptide and a smaller 10-kDa N-terminal fragment, confirmed by mass spectrometry (data not shown). To investigate the contribution of these subdomains to adhesion, we produced Fap1-NR_α and Fap1-NR_β separately in *E. coli* and tested their ability to block *S. parasanguinis* binding to SHA (Fig. 1*b*). Each domain shows a dose-dependent reduction in *S. parasanguinis* adhesion suggesting that they both play important roles in adhesion.

Structure of the Major Nonrepeat Region Fap1-NR—To explore the potential cooperative roles of Fap1-NR_α and Fap1-NR_β and to provide a better understanding of adhesion by Fap1, we embarked on a high resolution structural investigation. We initiated our structural studies using the intact 36-kDa Fap1-NR. Crystals of Fap1-NR were obtained after 1 day, between pH 6.5 and 8.5, with the highest resolution diffraction obtained for crystals grown at pH 8. Structure determination was undertaken using Se-SAD, and the electron density map was refined to 2.9 Å (Table 1 and supplemental Fig. S1). The β domain was built into the experimental electron density map from residues Thr-236 to Asp-435, although the electron density corresponding to all preceding residues was not observable. Crystals were washed and analyzed by SDS-PAGE, which showed no sign of degradation (data not shown); therefore, it was postulated that the lack of electron density for this portion of Fap1-NR results from significant disorder in the N-terminal region, which encompasses Fap1-NR_α. The final model contains two identical molecules of the β domain in a head-to-tail arrangement within the asymmetric unit. The dimer interface is small, consisting of only the short loop connecting β10 and β11 in the monomer structure (Fig. 2*a*), which implies that dimer formation is most likely an artifact of crystal packing. Gel filtration experiments also indicate that under these conditions Fap1-NR is largely monomeric in solution (supplemental Fig. S2). The β domain is

TABLE 2

NMR structural constraints and structure statistics for Fap1-NR_α

Summary of structural constraints and structure statistics (PDB code 2kub) are shown.

No. of restraints	
Distance restraints	
Intra-residue ($\|i-j\|=0$)	451
Sequential ($\|i-j\|=1$)	211
Medium range ($2 \le \|i-j\| < 5$)	256
Long range ($\|i-j\| \ge 5$)	103
Ambiguous	565
Total	1586
Dihedral angle restraints (φ/ψ)	138 (69/69)
Hydrogen bonds restraints	49
RDC restraints (D_{NH}/D_{CaHa})	38/54
Restraints statistics[a]	
r.m.s. of distance violations	
NOE restraints	0.11 ± 0.01 Å
H-bond restraints	0.06 ± 0.01 Å
r.m.s. of dihedral violations	0.25 ± 0.07°
RDC *Q*-factors	
D_{NH}	0.19 ± 0.04
D_{CaHa}	0.31 ± 0.01 Hz
r.m.s. from idealized covalent geometry	
Bonds	0.0029 ± 0.00008 Å
Angles	0.49 ± 0.009°
Impropers	1.45 ± 0.06°
Structural quality[a]	
Ramachandran statistics[b]	
Most favored regions	99.2 ± 0.9%
Allowed regions	0.8 ± 0.9%
Generously allowed regions	0 ± 0%
Disallowed regions	0 ± 0%
WHAT-IF Z-score[c]	
Backbone conformation	1.90 ± 0.18
2nd generation packing quality	4.32 ± 0.37
Ramachandran plot appearance	−0.82 ± 0.39
$\chi1/\chi2$ rotamer normality	−2.22 ± 0.17
Coordinates precision[d]	
All backbone atoms	0.39 ± 0.06 Å
All heavy atoms	0.81 ± 0.07 Å

[a] Average values and standard deviations over the 10 lowest energy conformers are shown.
[b] Percentage of residues in the Ramachandran plot regions was determined by PROCHECK (86).
[c] *Z*-scores values were reported by WHAT-IF (87).
[d] Average root mean square (r.m.s.) deviation (r.m.s.d.) over the 10 lowest energy conformer atomic coordinates with respect to the average structure are shown.

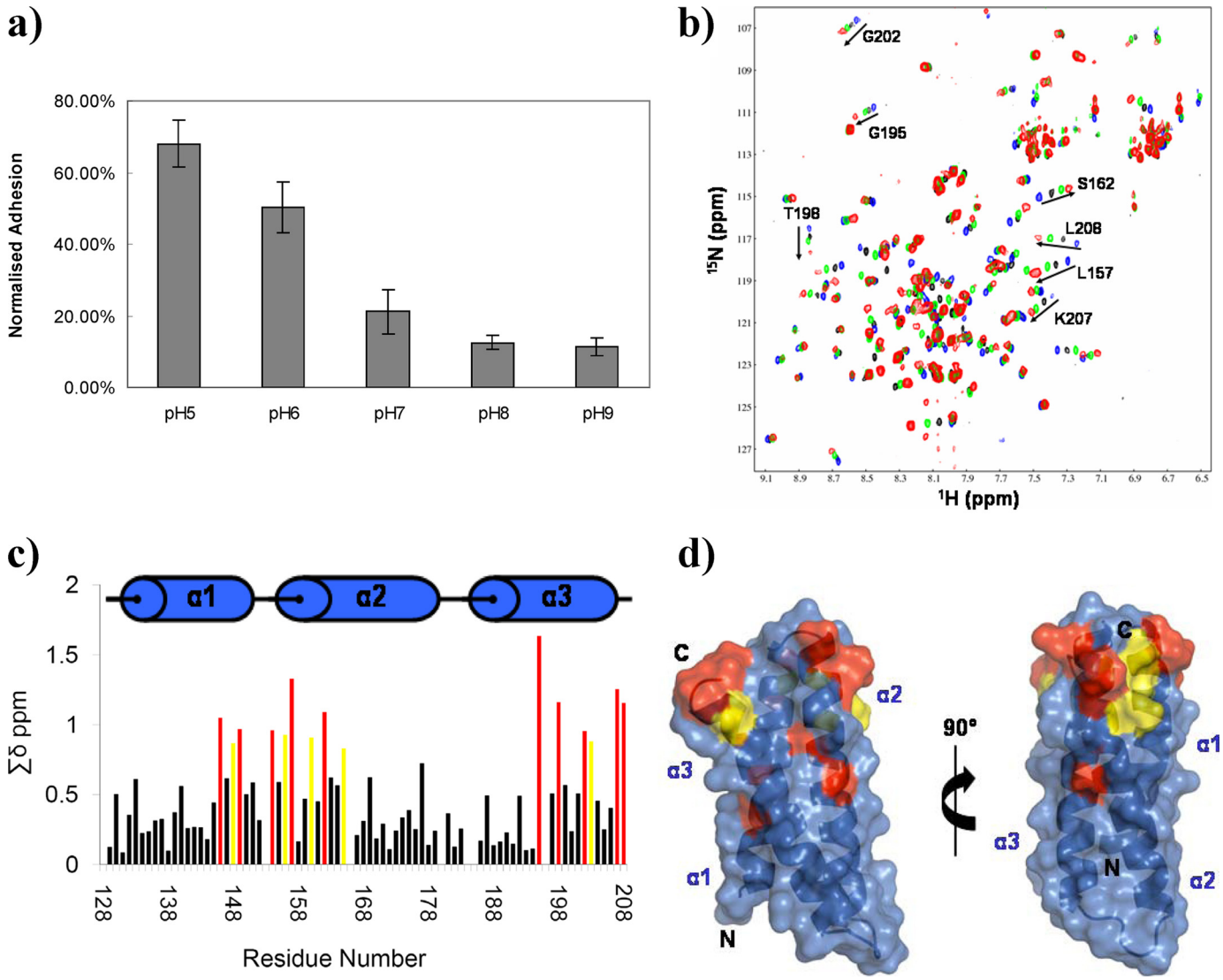

FIGURE 3. **pH-dependent structural change in Fap1-NR$_\alpha$.** *a, S. parasanguinis* adhesion to SHA is pH-dependent. Adhesion of ^{3}H-labeled wild-type bacteria to SHA was carried out at pH 5.0, 6.0, 7.0, 8.0, and 9.0. *b,* superimposition of regions from the ^{15}N-^{1}H HSQC spectra of Fap1-NR$_\alpha$ measured at 500 MHz at pH 8.0 (*blue*), pH 6.2 (*black*), pH 5.7 (*green*), and pH 5.2 (*red*). Full TROSY-HSQC spectra of Fap1-NR are shown in supplemental Fig. S7. *c,* weighted differences in the observed ^{1}H and ^{15}N chemical shifts of Fap1-NR$_\alpha$ between pH 8.0 and 5.2, where $\Sigma\delta$ ppm = $(4 \times \delta^1\text{H}) + \delta^{15}\text{N}$. Residues significantly affected by pH ($\Sigma\delta$ ppm $>$0.95) are highlighted in *red*, and those affected to a lesser extent (0.95 $<$ $\Sigma\delta$ ppm $>$ 0.8) are highlighted in *yellow*. The secondary structure of the helical bundle is shown at the top. More details are also given in supplemental Figs. S7 and S8. *d,* localization of the chemical shift changes between pH 8 and 5.2 on the NMR structure of Fap1-NR$_\alpha$ at pH 8. The three helices and the surface not affected by pH are in *blue*, although residues displaying chemical shift changes due to pH are colored in *red* (large) and *yellow* (small). The orientation is the same as Fig. 2*C*. The chemical shift changes are localized toward the C-terminal pole.

composed of 12 β-strands arranged in two extensive β-sheets built from four anti-parallel β-strands (Fig. 2, *a* and *b*). Four additional, short β-strands elaborate one face of the structure, creating an extended twisted β-platform. A striking feature is the presence of large loops protruding at the top (L1–L2–L5) and the bottom (L3–L6–L9) of the β-sandwich and obscuring the face of the extended β-sheet (Fig. 2, *a* and *b*, L4-L7-L8). These loops are well ordered and are stabilized through hydrophobic interactions with exposed aromatic residues from the β-sheet core structure. A series of hydrophobic residues within L1–L2–L5 form an exposed ledge on the top of the structure (supplemental Fig. S3).

The absence of electron density for the N terminus of Fap1-NR$_\alpha$ may be due to a lack of structural integrity or the presence of multiple, but ordered, conformations arising from flexibility within the 27-amino acid linker. To elucidate the structure of this domain, we used solution state NMR spectroscopy. Two-dimensional ^{1}H-^{15}N HSQC spectra display excellent dispersion in backbone amide chemical shifts at pH 8, consistent with a folded polypeptide (supplemental Fig. S4). The ^{15}N relaxation rates at pH 8 for backbone amides between Glu-128 and Leu-208 reveal a well ordered structure with no flexible loops or residues in chemical exchange, although the termini (residues 116–127 and 209–231) are highly flexible. Furthermore, NMR spectra indicate that Fap1-NR$_\alpha$ is monomeric at concentrations up to 300 μM, but it self-associates at higher concentrations (supplemental Fig. S5).

Using a combination of manual and ARIA NMR assignment methods for Fap1-NR$_\alpha$ (28, 29), a total of 1586 NOEs were assigned in Fap1-NR$_\alpha$ ^{15}N/^{13}C-edited NOESY spectra at pH 8.

The structure determination was supplemented with ϕ and φ dihedral angles and 92 residual dipolar coupling restraints (Table 2). All areas of secondary structure are well defined (Fig. 2*c*); the average pairwise root mean squared deviation for the water-refined final structures is 0.39 ± 0.06 Å for the backbone atoms and 0.81 ± 0.07 Å for the heavy atoms of residues within

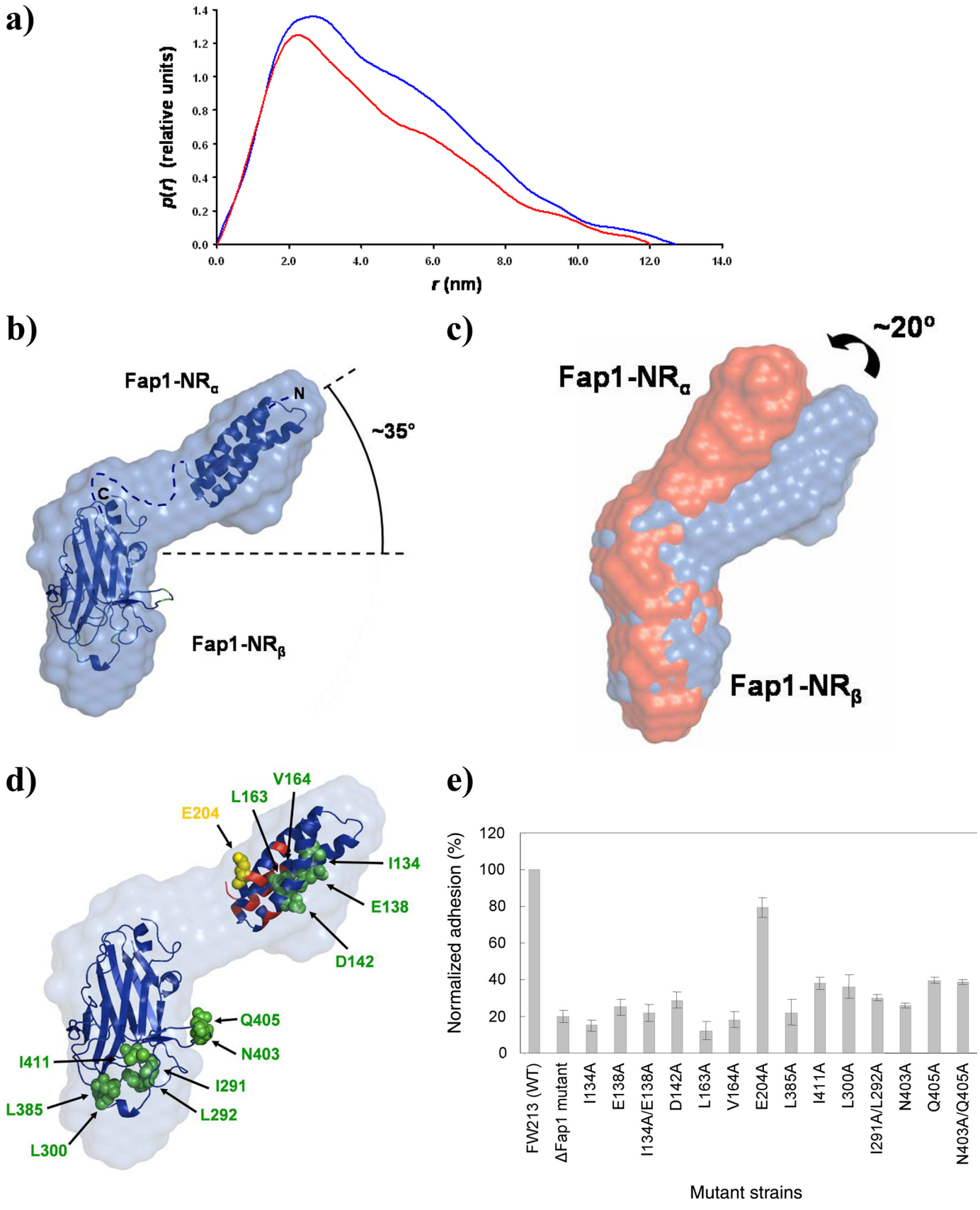

secondary structure. The final structure of the Fap1-NR$_\alpha$ exhibits an α-helical bundle topology (Fig. 2*c*), in which the three α-helices pack against each other in an up-down-up arrangement (α1 residues 129–150, α2 residues 153–178, and α3 residues 184–206). Hydrophobic interactions involving the side chains of leucine, alanine, and isoleucine residues stabilize the inter-helix interactions (Fig. 2*d*). Comparison of the ^{15}N-^{1}H TROSY HSQC of Fap1-NR with spectra of either Fap1-NR$_\alpha$ or Fap1-NR$_\beta$ indicates that although the majority of peaks for the isolated domains superimpose well with their counterparts for Fap1-NR, a limited number exhibit chemical shifts differences, suggesting the presence of a small interface between the domains (supplemental Fig. S4). Furthermore, differences in ^{15}N relaxation times for α and β domains within Fap1-NR indicate some interdomain flexibility (average T_1/T_2 ratios are 21 and 27 for α and β domains respectively; supplemental Fig. S5).

pH-dependent Conformational Change within Fap1—The oral cavity experiences a wide pH range, from neutrality at the normal saliva buffering conditions to values below 5.0, induced by the fermentation of ingested sugars by resident bacteria. To investigate the effect of pH on *S. parasanguinis* adhesion, SHA binding assays were repeated over a range of pH values. A progressive increase in adhesion was observed as the pH was lowered from alkaline (pH 8) to acidic (pH 5) conditions (Fig. 3*a*), whereas no change in basal adhesion for the *fap1* mutant strain was observed (supplemental Fig. S6). To characterize this further, two-dimensional ^{1}H-^{15}N TROSY-HSQC spectra of Fap1-NR were recorded over the same pH range (supplemental Fig. S7). Intriguingly, strong pH dependences were observed for many ^{1}H and ^{15}N chemical shifts of residues located within the α domain, whereas the majority of the residues from the β domain were not affected (supplemental Fig. S7). CD experiments performed between pH 5 and 8 indicate that the α-helical content remains unchanged over the pH range (data not shown). This was confirmed by repeating the pH titration and monitoring ^{1}H and ^{15}N chemical shifts of amides within the isolated Fap1-NR$_\alpha$ domain (Fig. 3*b*). After reassignment of the NMR spectra at pH 5, an analysis of backbone secondary shifts indicates that the three α-helices remain largely intact, consistent with CD measurements, and that no unfolding occurs between the pH 8 and 5. Amide chemical shift changes are localized to one end of the α-helical bundle (Fig. 3, *c* and *d*). Although no histidine residues are present, the Fap1-NR$_\alpha$ domain possesses 18 charged residues (12 acidic and 6 basic; supplemental Fig. S8). Interestingly, the amide resonances for three of these residues (Arg-146, Asp-152, Glu-154, and Lys-207) titrate with pH. Furthermore, chemical shift changes of several hydrophobic residues (Leu-148, Leu-151, Leu-157, Ala-165, Ile-206, and Leu-208) proximal to charged groups are also observed (supplemental Fig. S8). Decreasing the pH may cause a rearrangement of the relative orientation and/or dynamics of the α-helices.

TABLE 3
SAXS data collection, processing and modelling statistics

	pH 5	pH 8
***P*(*r*) function calculation**		
q range	0.018–0.464 Å^{-1}	0.021–0.464 Å^{-1}
R_g	35.0 ± 0.2 Å	36.2 ± 0.1 Å
$I(0)$	88.5 ± 0.3	108.4 ± 0.3
D_{max}	127 Å	128 Å
Estimated molecular mass[a]	31 kDa	38 kDa
Mass calculated from sequence	37 kDa	37 kDa
***Ab initio* GASBOR modeling**		
Ensemble average χ^2 to raw data	1.98 ± 0.07	2.15 ± 0.07
NSD[b]	1.11 ± 0.04	1.47 ± 0.07

[a] Normalization against data for BSA was calculated using the formula $(I(0)_{FAP} \div I(0)_{BSA} \cdot 66\ kDa)$, where $I(0)_{BSA}$ was 188.3.
[b] For the definition of normalized spatial discrepancy (NSD) (88).

SAXS provides useful low resolution information on the global structural features of proteins in solution. This technique is sensitive to changes in relative position of domains or positions of secondary structure and is therefore highly suitable for determining the overall structure of Fap1-NR under acidic and alkaline conditions. After exhaustive gel filtration chromatography of recombinant Fap1-NR at pH 8 and 5, SAXS measurements were recorded (Fig. 4, *a* and *b*; Table 3). The resulting SAXS density indicates that Fap1-NR exists as a curved, extended structure consisting of two domains (Fig. 4*b*). The relative sizes of Fap1-NR$_\alpha$ and Fap1-NR$_\beta$ domains are consistent with two halves of the density. Comparison of the data at pH 8 and 5 reveals a subtle difference in conformation, as judged by a change in the shape of the pair-distance distribution function (Fig. 4*a*). Upon reducing the pH, the pair-distance distribution shifts to longer distances, for which a plausible interpretation would be an opening of the two-domain structure (Fig. 4*c*). It is also likely that the extent of interdomain mobility is affected by pH and would contribute to an altered SAXS profile. It is interesting to note that the residues affected by the change in pH within the α domain would be situated adjacent to the 27-residue linker between Fap1-NR$_\alpha$ and Fap1-NR$_\beta$ (Fig. 4*d*).

Analysis of the atomic resolution details of Fap1-NR reveals two patches on the surfaces of the α and β domains that include a number of exposed hydrophobic side chains (Fig. 4*d*). The exposed hydrophobic residues together with selected adjacent residues within these regions were selected for mutation; these include five amino acids in Fap1-NR$_\alpha$ (Ile-134, Glu-138, Asp-

FIGURE 4. **Overall structure of Fap1-NR and mutagenesis.** *a,* SAXS scattering profile of Fap1-NR at pH 5 (*red*) and pH 8 (*blue*). *b,* SAXS-derived electron density for Fap1-NR at pH 8 with the crystal structure of Fap1-NR$_\beta$ and the solution structure of Fap1-NR$_\alpha$ rigid body fitted into the envelope. The 27-residue linker is shown as a *blue dashed line* and the N and C termini of Fap1-NR are annotated. *c,* effects of pH change on the electron density of Fap1-NR. SAXS derived electron density at pH 8 is *blue* and at pH 5 is *red*. *d,* potential receptor binding surface of Fap1. Two exposed hydrophobic regions were mutated Fap1-NR. Residues, including Ile-134, Glu-138, Asp-142, Leu-163, and Val-164 in Fap1-NR$_\alpha$ together with Leu-385, Ile-291, Leu-292, Leu-300, Asn-403, Gln-405, and Ile-411 in Fap1-NR$_\beta$, were mutated to alanine. Mutants affecting adhesion of Fap1-NR are shown as *green spheres* and line the concave face of the SAXS envelope. The position of the negative control E204A is shown as *yellow spheres* and is on the nonconcave face. Residues in Fap1-NR$_\alpha$ affected by changes in pH are colored *red* and congregate at the interdomain boundary. *e,* effect of site-directed mutagenesis of amino acid residues located at the putative binding interfaces in Fap1-NR on bacterial adhesion to SHA. Adhesion of *S. parasanguinis* FW213 (*1st column*), *fap1* mutant (*2nd column*), and site-directed *fap1* mutants as follows: I134A (*3rd column*), E138A (*4th column*), I134A/E138A (*5th column*), D142A (*6th column*), L163A (*7th column*), V164A (*8th column*), and E204A (*9th column*), in the α domain; and L385A (*10th column*), I411A (*11th column*), L300A (*12th column*), I291A/L292A (*13th column*), N403A (*14th column*), Q405A (*15th column*), and N403A/Q405A (*16th column*) in the β domain.

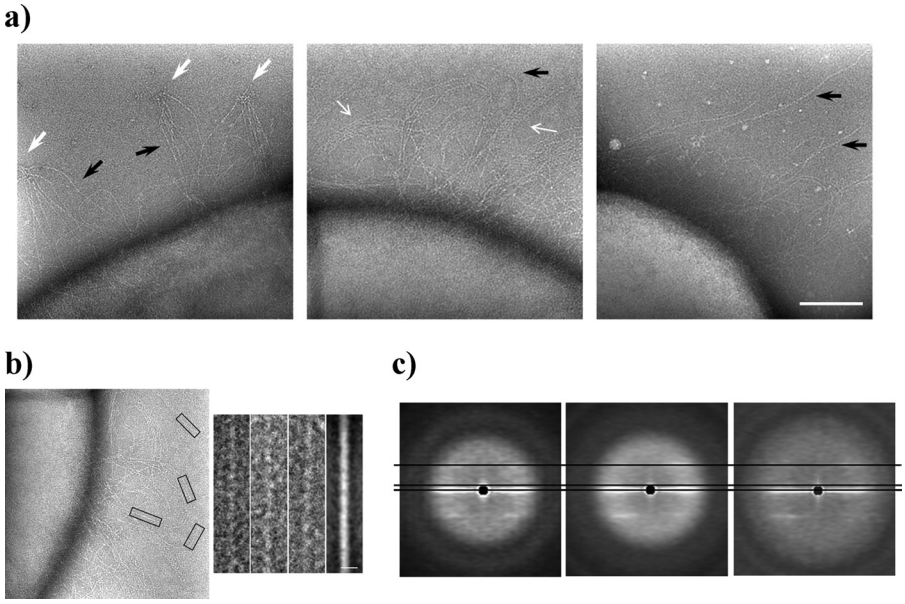

FIGURE 5. **Electron microscopy of Fap1 fimbriae.** *a,* micrographs of long fimbriae from wild-type *S. parasanguinis* stained with UA (*left*), PTA (*center*), and MAT (*right*). *Scale bar,* 100 nm. *Black arrows* indicate fimbriae; *white arrows* indicate tip aggregates; *open white arrows* indicate fimbrial bundles. *b,* averaging of narrow fimbrial sections; micrograph of *S. parasanguinis* stained with PTA (*left*), three representative fimbrial sections (*center*), and average of all fimbrial regions (*right*). *Scale bar,* 10 nm. Fimbriae diameter 5.5 nm. *c,* average power spectra from fimbrial regions stained with UA (*left*), PTA (*middle*), and MAT (*right*) lines show the principal 1/6.5 nm layer line and a weaker one at 1/33 nm, present in all staining conditions.

142, Leu-163, and Val-164) and seven amino acids located within the hydrophobic patch within L1–L2 and L5 in Fap1-NR$_\beta$ (Leu-385, Ile-291, Leu-292, Leu-300, Asn-403, Gln-405, and Ile-411) (Fig. 2, *a* and *b*; Fig. 4*d,* and supplemental Fig. S3). We hypothesized that these residues may form part of a binding site for the salivary pellicle, and we created a series of site-specific Fap1 mutants in this region within *S. parasanguinis* and measured their ability to adhere to SHA (Fig. 4*e*). As a control, a charge mutation at Fap1-E204A on the opposite face of the α domain was also constructed and tested. Western blot analysis revealed that all the mutants expressed Fap1 (data not shown); however, all exhibited deficiencies in bacterial adhesion with the exception E204A.

Overall Structure of Fap1—We analyzed the feasibility of imaging the fimbriae on the bacterial surface of the wild-type strain (FW213) for structure determination by single particle electron microscopy using several negatively stained preparations. Good results were obtained with preparations in 1% UA, 2% PTA, pH 7, and 2% MAT (Fig. 5*a*). The fimbriae are very flexible structures that bend easily in all the preparations. A close look at individual fimbriae reveals a diameter of ~5.5 nm and an internal substructure with a periodicity of ~6.5 nm. At neutral pH, fimbriae are close together forming rafts, and the internal substructure is more apparent (Fig. 5*a*, *open white arrows*). At low pH (UA staining), the tip of the fimbriae come together to form aggregates (Fig. 5*a*, *white arrows*), in which the adhesion points are located uniquely at the tip of the fimbriae. Strikingly, despite the fimbriae being more abundant on the cell surface at pH 7.0 using staining reagents PTA and MAT, the tips do not come together. Even though an additional contribution from the electrostatic charges of the different stains at the experimental pH cannot be ruled out at the present time, these data support the notion of a pH-dependent conformational change for Fap1.

Once electron micrographs of whole-mount bacterial preparations in different negative stains had been collected, digitized, and corrected for the contrast transfer function of the microscope, fimbrial regions were extracted from the images following strict criteria; the fimbriae should be straight; they should not overlap other fimbriae, and they should be separated by at least two fimbrial diameters from its nearest neighbor (Fig. 5*b*). As many images as possible, with a length of ~55 nm, were extracted from the boxed fimbrial regions. After centering the images, an average image (Fig. 5*b*) and an average power spectrum (Fig. 5*c*) were calculated for each staining condition. The power spectra, in all stain preparations, show predominant layer lines at 1/(6.5 nm) and 1/(33 nm), which relate to structural repeats in the fimbriae. At the present time, an unambiguous assignment of the Bessel orders is not possible due to the weak scattering power of the fimbrial regions and the uncertainty in the diameter of fimbriae.

DISCUSSION

Recent studies have suggested that Fap1 belongs to a wider family of cell wall-anchored, serine-rich repeat proteins (49) that exhibit features distinct from the pili of other Gram-positive organisms, such as *Corynebacteria diphtheria*, group A and group B *Streptococcus* (GAS and GBS), and Gram-negative bacteria expressing chaperone usher and type IV secretion systems. Typically, these pili are characterized by small subunits noncovalently or covalently linked to each other (54–56), whereas SRR fimbriae are characterized by the presence of extensive glycosylated serine-rich repeats within a large protein subunit (>200 kDa). SSR fimbriae are found on several pathogenic streptococci and staphylococci, which include GspB from *Streptococcus gordonii* (17), SSR-1 and SSR-2 from *Streptococcus agalactiae* (21, 22, 57), SrpA from *S. sanguinis* (50), and SraP from *Staphylococcus aureus* (18). Many of these proteins mediate specific interactions with human platelets through their N-terminal regions, which share little sequence homology to each other and are implicated in binding to a diverse array of host receptors (20, 57).

We have demonstrated that a 36-kDa fragment from the nonrepeat region of Fap1 (Fap1-NR) harbors the binding properties for colonization of the oral cavity (58). Fap1-NR includes two domains with distinct secondary structure and topology, namely an α-helical domain (residues 116–231, Fap1-NR$_\alpha$; Fig. 1*a*) and another composed predominantly of β-strands (residues 231–437, Fap1-NR$_\beta$; Fig. 1*a*). The protein sequence out-

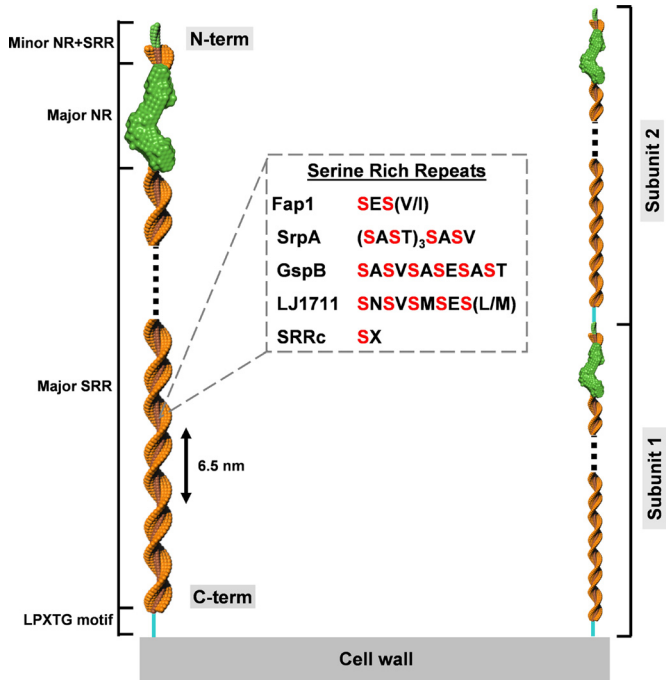

FIGURE 6. **Model for the super-coiled strand of Fap1 fimbriae.** The protomer is colored as in Fig. 1*a* with the cell wall anchor colored *cyan*, the major and minor SRR regions colored *dark* (protein) and *light* (glycan) *orange*, although the major and minor NR regions are colored *green*. The model on the *left* represents a super-coiled Fap1 monomer with repeating units of 6.5 nm along the fiber axis of the SRR region and protomer length of ~250–300 nm. Extra subunits may be incorporated within a coiled-coil to produce higher oligomeric states, and the model on the *right* represents multiple polymerized subunits with just two displayed here. The Fap1 model was created from a left-handed helix in which single atoms (representing individual amino acids) were arranged on a helical axis, with additional atoms (representing glycan residues) associated with alternate amino acid residues. This helix was in turn rotated about a central super-helical fiber axis. The SAXS envelope was scaled to the SRR model and placed at the C termini, followed by a short stretch of the helical SRR model representing the minor SRR. An alignment of SRR sequences (*middle*) from *S. parasanguinis* Fap1, *S. aureus* SrpA, *S. gordonii* M99 GspB, and *Lactobacillus johnsonii* NCC533 LJ1711 is shown. The consensus SRR dipeptide sequence (*SRRc*) is *SX*, where *X* can be any amino acid.

side the nonrepeat region is composed of ~2000 amino acid residues of S(V/I/E) dipeptide repeats. Perfect sequence repeats of less than four amino acids tend to form fibrous extended structures that are often super-helical (59), for example the collagen triple helix (60), the zigzag β-structure of the silk I (61, 62), and the β-turn helix of the *Plasmodium falciparum* circumsporozoite protein (63, 64). The extensive repetition of the serine dipeptides together with our electron microscopy data suggest a model for the fimbriae in which Fap1 strands form a super-helical extended structure with a principal repeat at 6.5 nm and serine side chains exposed for *O*-glycosylation (Fig. 6). The larger 33 nm periodicity may be attributed to an independent helical stripe of surface glycosylation, the exact pattern of which has yet to be determined. Furthermore, because there is an ambiguity in layer line indexing, fimbriae consisting of a coiled coil arrangement of two or more Fap1 helical strands cannot be excluded. Fap1 fimbriae are variable in length (in 300–600 μm range), similar to other SRR fibrils, *e.g.* SrpA on the surface of *Streptococcus cristatus* (65). These length variations could be attributed to more than one subunit present per fimbriae, linked in a head-to-tail fashion. Although the classic pilin motif for head-to-tail cross-linking is absent (56, 66), lysines residues present at the N terminus of Fap1 could act as substrates for this cross-linkage.

In this model, the N-terminal nonrepeat domain, Fap1-NR, includes two globular domains that are located at the distal end of the structure for adhesion. Although no significant primary sequence similarity can be detected with proteins of known structure (no e value <1 PHYRE hits (67)), both domains display structural similarity to two separate families of surface proteins from Gram-positive bacteria (68). The structure of the β domain resembles the ligand-binding A-region from the Microbial Surface Components Recognizing Adhesive Matrix Molecules (MSCRAMM) family of bacterial adhesins (supplemental Fig. S8*a*). Specifically, a high degree of similarity is observed with the fibrinogen-binding protein SdrG from *Staphylococcus epidermidis* (PDB code 1r17; supplemental Fig. S8*a*) (55, 69, 70), the collagen-binding adhesin from *Enterococcus faecalis* (PDB code 2z1p; supplemental Fig. S8*b*) (71, 72), and the clumping factor A from *S. aureus* (PDB code 1n67; supplemental Fig. S8*c*) (73–75), typically with a backbone root mean squared deviation of 3.5 Å over ~120 residues. The MSCRAMM ligand-binding region encompasses two similar β domains, in which a ligand peptide docks into an interdomain groove of the open structure and a C-terminal extension closes the complex resulting in a change in relative domain orientation (74). Although the α domain is unrelated to the flanking β-rich domain from the MSCRAMMs, it displays a striking similarity with the imperfect helical repeats of EBH, the giant, extracellular matrix-binding protein from staphylococci (PDB code 2dgj; supplemental Fig. S8*d*) (76). The lack of electron density for the α domain within the crystal structure of Fap1-NR, coupled with its well defined structure in solution, also implies that some flexibility exists at the interdomain boundary. It is tempting to speculate that the dual similarity with EBH and MSCRAMM surface proteins implies that host extracellular matrix proteins are putative targets for Fap1 and supports the wider role for SRR fimbriae. The interaction between Fap1 and the salivary pellicle also suggests a role for calcium binding; however, no direct interaction was observable in our NMR assays (data not shown).

Fap1 exhibits an unusual pH-dependent conformational change that affects key residues located at the interdomain junction of the two subdomains of Fap1-NR, with concomitant effects on the relative arrangement of these domains that allow Fap1 to adhere more tightly to SHA. The mean resting saliva pH observed in human oral cavities lies in the range 6.5 to 7.1. However, the buffering capacity of saliva is unable to cope with the rapid drop in pH induced by microbial acid production after the ingestion of fermentable carbohydrates. Plaque pH can reach values below 5.0 and remain low for some time before returning to neutrality. Some streptococci, particularly *S. mutans*, alter their physiology to survive in acidic environments. This is known as the acid tolerance response and includes the production of stress-responsive proteins, increased glycolytic activity, and the regulation of intracellular pH (77, 78). *S. parasanguinis* and many other oral streptococci are primary colonizers of the oral cavity and will frequently be exposed to acidic stress; however, they are unable to thrive at low pH and

in response shut down their metabolic functions (79). A plausible mechanism for survival would be for *S. parasanguinis* to modulate adhesion to outcompete acid-tolerant species, a mechanism that has been proposed for other species of bacteria (80–84). Enhanced Fap1-mediated adhesion at low pH would provide a more tenacious attachment to the salivary pellicle and increase the likelihood of *S. parasanguinis* survival during periods of acidic conditions. Moreover, its role as substrate for biofilm formation would also be enhanced thereby increasing bacterial cell density and providing respite.

Using a combination of low and high resolution methods, we provide new insights into the architecture of Fap1 fimbriae and adhesion by a primary colonizer of the human oral cavity. Furthermore, our conclusions likely extend to other SRR fimbriae from pathogenic organisms and suggest new therapeutic strategies.

Acknowledgments—We thank the beamline scientists at ID29 of the European Synchrotron Radiation Facility and X33 at the DORIS-III ring of the Deutsches Elektronen-Synchrotron. We are also indebted to Christina Redfield at Oxford University for the provision of 950 MHz instrument time. The 950 MHz NMR facility was funded by the Wellcome Trust Joint Infrastructure Fund and the E. P. Abraham Fund.

REFERENCES

1. Fux, C. A., Costerton, J. W., Stewart, P. S., and Stoodley, P. (2005) *Trends Microbiol.* **13,** 34–40
2. Mandlik, A., Swierczynski, A., Das, A., and Ton-That, H. (2008) *Trends Microbiol.* **16,** 33–40
3. Costerton, J. W., Stewart, P. S., and Greenberg, E. P. (1999) *Science* **284,** 1318–1322
4. Nobbs, A. H., Lamont, R. J., and Jenkinson, H. F. (2009) *Microbiol. Mol. Biol. Rev.* **73,** 407–450
5. Kreth, J., Merritt, J., and Qi, F. (2009) *DNA Cell Biol.* **28,** 397–403
6. Paju, S., and Scannapieco, F. A. (2007) *Oral Dis.* **13,** 508–512
7. Scannapieco, F. A., Bush, R. B., and Paju, S. (2003) *Ann. Periodontol.* **8,** 38–53
8. Fujitani, S., Rowlinson, M. C., and George, W. L. (2008) *Clin. Infect. Dis.* **46,** 1064–1066
9. Giannitsioti, E., Chirouze, C., Bouvet, A., Béguinot, I., Delahaye, F., Mainardi, J. L., Celard, M., Mihaila-Amrouche, L., Moing, V. L., Hoen, B., and Grp, A. S. (2007) *Clin. Microbiol. Infect.* **13,** 770–776
10. Westling, K., Julander, I., Ljungman, P., Jalal, S., Nord, C. E., and Wretlind, B. (2006) *Int. J. Antimicrob. Agents* **28,** 292–296
11. Stephenson, A. E., Wu, H., Novak, J., Tomana, M., Mintz, K., and Fives-Taylor, P. (2002) *Mol. Microbiol.* **43,** 147–157
12. Wu, H., and Fives-Taylor, P. M. (1999) *Mol. Microbiol.* **34,** 1070–1081
13. Zhou, M., Peng, Z., Fives-Taylor, P., and Wu, H. (2008) *Infect. Immun.* **76,** 5624–5631
14. Wu, H., Mintz, K. P., Ladha, M., and Fives-Taylor, P. M. (1998) *Mol. Microbiol.* **28,** 487–500
15. Froeliger, E. H., and Fives-Taylor, P. (2001) *Infect. Immun.* **69,** 2512–2519
16. Rigel, N. W., and Braunstein, M. (2008) *Mol. Microbiol.* **69,** 291–302
17. Xiong, Y. Q., Bensing, B. A., Bayer, A. S., Chambers, H. F., and Sullam, P. M. (2008) *Microb. Pathog.* **45,** 297–301
18. Siboo, I. R., Chambers, H. F., and Sullam, P. M. (2005) *Infect. Immun.* **73,** 2273–2280
19. van Sorge, N. M., Quach, D., Gurney, M. A., Sullam, P. M., Nizet, V., and Doran, K. S. (2009) *J. Infect. Dis.* **199,** 1479–1487
20. Shivshankar, P., Sanchez, C., Rose, L. F., and Orihuela, C. J. (2009) *Mol. Microbiol.* **73,** 663–679
21. Mistou, M. Y., Dramsi, S., Brega, S., Poyart, C., and Trieu-Cuot, P. (2009) *J. Bacteriol.* **191,** 4195–4206
22. Seifert, K. N., Adderson, E. E., Whiting, A. A., Bohnsack, J. F., Crowley, P. J., and Brady, L. J. (2006) *Microbiology* **152,** 1029–1040
23. Sattler, M., Schleucher, J., and Griesinger, C. (1999) *Prog. NMR Spectroscopy* **34,** 93–158
24. Ottiger, M., Delaglio, F., and Bax, A. (1998) *J. Magn. Reson.* **131,** 373–378
25. Pervushin, K., Riek, R., Wider, G., and Wüthrich, K. (1997) *Proc. Natl. Acad. Sci. U.S.A.* **94,** 12366–12371
26. Delaglio, F., Grzesiek, S., Vuister, G. W., Zhu, G., Pfeifer, J., and Bax, A. (1995) *J. Biomol. NMR* **6,** 277–293
27. Johnson, B. A., and Blevins, R. A. (1994) *J. Biomol. NMR* **4,** 603–614
28. Bardiaux, B., Bernard, A., Rieping, W., Habeck, M., Malliavin, T. E., and Nilges, M. (2009) *Proteins* **75,** 569–585
29. Rieping, W., Habeck, M., Bardiaux, B., Bernard, A., Malliavin, T. E., and Nilges, M. (2007) *Bioinformatics* **23,** 381–382
30. Brünger, A. T., Adams, P. D., Clore, G. M., DeLano, W. L., Gros, P., Grosse-Kunstleve, R. W., Jiang, J. S., Kuszewski, J., Nilges, M., Pannu, N. S., Read, R. J., Rice, L. M., Simonson, T., and Warren, G. L. (1998) *Acta Crystallogr. D Biol. Crystallogr.* **54,** 905–921
31. Cornilescu, G., Delaglio, F., and Bax, A. (1999) *J. Biomol. NMR* **13,** 289–302
32. Clore, G. M., Gronenborn, A. M., and Bax, A. (1998) *J. Magn. Reson.* **133,** 216–221
33. Dosset, P., Hus, J. C., Marion, D., and Blackledge, M. (2001) *J. Biomol. NMR* **20,** 223–231
34. Nilges, M., Bernard, A., Bardiaux, B., Malliavin, T., Habeck, M., and Rieping, W. (2008) *Structure* **16,** 1305–1312
35. Linge, J. P., Habeck, M., Rieping, W., and Nilges, M. (2003) *Bioinformatics* **19,** 315–316
36. Collaborative Computational Project No. 4 (1994) *Acta Crystallogr. D Biol. Crystallogr.* **50,** 760–763
37. Schneider, T. R., and Sheldrick, G. M. (2002) *Acta Crystallogr. D Biol. Crystallogr.* **58,** 1772–1779
38. Emsley, P., and Cowtan, K. (2004) *Acta Crystallogr. D Biol. Crystallogr.* **60,** 2126–2132
39. Murshudov, G. N., Vagin, A. A., and Dodson, E. J. (1997) *Acta Crystallogr. D Biol. Crystallogr.* **53,** 240–255
40. Konarev, P. V., Volkov, V. V., Sokolova, A. V., Koch, M. H., and Svergun, D. I. (2003) *J. Appl. Crystallogr.* **36,** 1277–1282
41. Petoukhov, M. V., and Svergun, D. I. (2003) *J. Appl. Crystallogr.* **36,** 540–544
42. Wriggers, W., and Chacón, P. (2001) *J. Appl. Crystallogr.* **34,** 773–776
43. Miller, D. J., Jerga, A., Rock, C. O., and White, S. W. (2008) *Structure* **16,** 1036–1046
44. Fives-Taylor, P. M., and Thompson, D. W. (1985) *Infect. Immun.* **47,** 752–759
45. Ruiz, T., Mechin, I., Bär, J., Rypniewski, W., Kopperschläger, G., and Radermacher, M. (2003) *J. Struct. Biol.* **143,** 124–134
46. Frank, J., Radermacher, M., Penczek, P., Zhu, J., Li, Y., Ladjadj, M., and Leith, A. (1996) *J. Struct. Biol.* **116,** 190–199
47. Radermacher, M., Ruiz, T., Wieczorek, H., and Grüber, G. (2001) *J. Struct. Biol.* **135,** 26–37
48. Ludtke, S. J., Baldwin, P. R., and Chiu, W. (1999) *J. Struct. Biol.* **128,** 82–97
49. Zhou, M., and Wu, H. (2009) *Microbiology* **155,** 317–327
50. Plummer, C., Wu, H., Kerrigan, S. W., Meade, G., Cox, D., and Ian Douglas, C. W. (2005) *Br. J. Haematol.* **129,** 101–109
51. Takamatsu, D., Bensing, B. A., Cheng, H., Jarvis, G. A., Siboo, I. R., López, J. A., Griffiss, J. M., and Sullam, P. M. (2005) *Mol. Microbiol.* **58,** 380–392
52. Takamatsu, D., Bensing, B. A., Prakobphol, A., Fisher, S. J., and Sullam, P. M. (2006) *Infect. Immun.* **74,** 1933–1940
53. Wu, H., Bu, S., Newell, P., Chen, Q., and Fives-Taylor, P. (2007) *J. Bacteriol.* **189,** 1390–1398
54. Fronzes, R., Remaut, H., and Waksman, G. (2008) *EMBO J.* **27,** 2271–2280
55. Bowden, M. G., Heuck, A. P., Ponnuraj, K., Kolosova, E., Choe, D., Gurusiddappa, S., Narayana, S. V., Johnson, A. E., and Höök, M. (2008) *J. Biol. Chem.* **283,** 638–647
56. Ton-That, H., and Schneewind, O. (2004) *Trends Microbiol.* **12,** 228–234
57. Samen, U., Eikmanns, B. J., Reinscheid, D. J., and Borges, F. (2007) *Infect. Immun.* **75,** 5405–5414

58. Wu, H., Zeng, M., and Fives-Taylor, P. (2007) *Infect. Immun.* **75,** 2181–2188
59. Kajava, A. V. (2001) *J. Struct. Biol.* **134,** 132–144
60. Shoulders, M. D., and Raines, R. T. (2009) *Annu. Rev. Biochem.* **78,** 929–958
61. Asakura, T., Ohgo, K., Komatsu, K., Kanenari, M., and Okuyama, K. (2005) *Macromolecules* **38,** 7397–7403
62. Sangappa, E. Y., Mahesh, S. S., and Somashekar, R. (2005) *J. Biosci.* **30,** 259–268
63. Ghasparian, A., Moehle, K., Linden, A., and Robinson, J. A. (2006) *Chem. Commun.* **2,** 174–176
64. Plassmeyer, M. L., Reiter, K., Shimp, R. L., Jr., Kotova, S., Smith, P. D., Hurt, D. E., House, B., Zou, X., Zhang, Y., Hickman, M., Uchime, O., Herrera, R., Nguyen, V., Glen, J., Lebowitz, J., Jin, A. J., Miller, L. H., MacDonald, N. J., Wu, Y., and Narum, D. L. (2009) *J. Biol. Chem.* **284,** 26951–26963
65. Handley, P. S., Correia, F. F., Russell, K., Rosan, B., and DiRienzo, J. M. (2005) *Oral Microbiol. Immunol.* **20,** 131–140
66. Hilleringmann, M., Ringler, P., Müller, S. A., De Angelis, G., Rappuoli, R., Ferlenghi, I., and Engel, A. (2009) *EMBO J.* **28,** 3921–3930
67. Kelley, L. A., and Sternberg, M. J. (2009) *Nat. Protocols* **4,** 363–371
68. Holm, L., Kääriäinen, S., Rosenström, P., and Schenkel, A. (2008) *Bioinformatics* **24,** 2780–2781
69. Ponnuraj, K., Bowden, M. G., Davis, S., Gurusiddappa, S., Moore, D., Choe, D., Xu, Y., Hook, M., and Narayana, S. V. (2003) *Cell* **115,** 217–228
70. Hartford, O., O'Brien, L., Schofield, K., Wells, J., and Foster, T. J. (2001) *Microbiology* **147,** 2545–2552
71. Sillanpää, J., Nallapareddy, S. R., Houston, J., Ganesh, V. K., Bourgogne, A., Singh, K. V., Murray, B. E., and Höök, M. (2009) *Microbiology* **155,** 2390–2400
72. Liu, Q., Ponnuraj, K., Xu, Y., Ganesh, V. K., Sillanpää, J., Murray, B. E., Narayana, S. V., and Höök, M. (2007) *J. Biol. Chem.* **282,** 19629–19637
73. Deivanayagam, C. C., Wann, E. R., Chen, W., Carson, M., Rajashankar, K. R., Höök, M., and Narayana, S. V. (2002) *EMBO J.* **21,** 6660–6672
74. Ganesh, V. K., Rivera, J. J., Smeds, E., Ko, Y. P., Bowden, M. G., Wann, E. R., Gurusiddappa, S., Fitzgerald, J. R., and Hook, M. (2008) *PloS Pathog.* **4,** e1000226
75. Keane, F. M., Loughman, A., Valtulina, V., Brennan, M., Speziale, P., and Foster, T. J. (2007) *Mol. Microbiol.* **63,** 711–723
76. Tanaka, Y., Sakamoto, S., Kuroda, M., Goda, S., Gao, Y. G., Tsumoto, K., Hiragi, Y., Yao, M., Watanabe, N., Ohta, T., and Tanaka, I. (2008) *Structure* **16,** 488–496
77. Takahashi, N., and Yamada, T. (1999) *Oral Microbiol. Immunol.* **14,** 43–48
78. Welin-Neilands, J., and Svensäter, G. (2007) *Appl. Environ. Microbiol.* **73,** 5633–5638
79. Svensäter, G., Larsson, U. B., Greif, E. C., Cvitkovitch, D. G., and Hamilton, I. R. (1997) *Oral Microbiol. Immunol.* **12,** 266–273
80. Brooks, D. E., and Trust, T. J. (1983) *J. Gen. Microbiol.* **129,** 3661–3669
81. Guglielmetti, S., Tamagnini, I., Minuzzo, M., Arioli, S., Parini, C., Comelli, E., and Mora, D. (2009) *Curr. Microbiol.* **59,** 167–172
82. Ito, H. O., Soutome, S., and Inoue, M. (2003) *J. Microbiol. Methods* **55,** 29–34
83. Kim, S. B., Park, S. J., Lee, C. G., Choi, N. C., and Kim, D. J. (2008) *Colloids and Surfaces B-Biointerfaces* **63,** 236–242
84. Takai, S., Yanagawa, R., and Kitamura, Y. (1980) *Infect. Immun.* **28,** 669–674
85. Davis, I. W., Leaver-Fay, A., Chen, V. B., Block, J. N., Kapral, G. J., Wang, X., Murray, L. W., Arendall, W. B., Snoeyink, J., Richardson, J. S., and Richardson, D. C. (2007) *Nucleic Acids Res.* **35,** 375–383
86. Laskowski, R. A., Macarthur, M. W., Moss, D. S., and Thornton, J. M. (1993) *J. Appl. Crystallogr.* **26,** 283–291
87. Vriend, G. (1990) *J. Mol. Graph.* **8,** 52–56, 29
88. Kozin, M. B., and Svergun, D. I. (2001) *J. Appl. Crystallogr.* **34,** 33–41

Structural Insights into Serine-rich Fimbriae from Gram-positive Bacteria

Stéphanie Ramboarina, James A. Garnett, Meixian Zhou, Yuebin Li, Zhixiang Peng, Jonathan D. Taylor, Wei-chao Lee, Andrew Bodey, James W. Murray, Yilmaz Alguel, Julien Bergeron, Benjamin Bardiaux, Elizabeth Sawyer, Rivka Isaacson, Camille Tagliaferri, Ernesto Cota, Michael Nilges, Peter Simpson, Teresa Ruiz, Hui Wu and Stephen Matthews

J. Biol. Chem. 2010, 285:32446-32457.
doi: 10.1074/jbc.M110.128165 originally published online June 28, 2010
